ORIGINAL PAPER

Magnetically recoverable iron oxide–hydroxyapatite nanocomposites for lead removal

H. Yang · S. Masse · M. Rouelle · E. Aubry · Y. Li · C. Roux · Y. Journaux · L. Li · T. Coradin

Abstract Magnetite–hydroxyapatite nanocomposites were prepared by in situ precipitation of the calcium phosphate phase in an iron oxide colloidal suspension. Homogeneous magnetic powders were obtained with iron oxide content up to 50 wt%, without perturbation of the magnetite structure nor formation of additional calcium phosphates. The surface area of the composite powder was significantly increased after incorporation of magnetite due to the better apatite particle dispersion. This results in an increased available reactive surface, favoring lead sorption and hydroxypyromorphite precipitation, both leading to an enhanced lead removal capacity of the composite materials. The magnetic properties of magnetite nanocrystals were preserved upon association with hydroxyapatite. Full recovery of the composite powder after lead removal could be achieved using a simple magnet at a relatively low iron oxide content (20 wt%). This indicates a strong interaction between hydroxyapatite and magnetite particles within the composite powder. The procedure is simple, easily scalable and involves only environmental friendly materials.

Keywords Hydroxyapatite · Magnetic materials · Nanoparticles · Lead

H. Yang · S. Masse · C. Roux · T. Coradin (✉)
Sorbonne Universités, UPMC Univ Paris 06, CNRS, Collège de France, UMR 7574, Chimie de la Matière Condensée de Paris, 75005 Paris, France
e-mail: thibaud.coradin@upmc.fr

H. Yang · L. Li
Key Laboratory of Cryogenics, Technical Institute of Physics and Chemistry, Chinese Academy of Sciences, Beijing 100190, People Republic of China

M. Rouelle · E. Aubry
Sorbonne Universités, UPMC Univ Paris 06, CNRS, UMR 7618, Biologie et Ecologie des Milieux Continentaux, 75005 Paris, France

Y. Li · Y. Journaux
Sorbonne Universités, UPMC Univ Paris 06, CNRS, UMR 7201, Institut Parisien de Chimie Moléculaire, 75005 Paris, France

Introduction

The concept of magnetically induced coagulation of sewage as a remediation technique was introduced in the early 1990s using magnetite nanoparticles (Booker et al. 1991), and several composite approaches involving sand, activated carbons, clays, zeolites and silica have been described since then (Benjamin et al. 1996; Oliveira et al. 2002; Oliveira et al. 2003; Oliveira et al. 2004). In this context, magnetic apatites obtained by association of iron oxide phases with hydroxyapatite have recently attracted attention, because they could offer the possibility for an easy and efficient recovery of the sorbent phase after treatment of contaminated waters (Dong et al. 2010). Hydroxyapatite $Ca_{10}(PO_4)_6(OH)_2$ has long been considered as one of the most promising mineral phases for remediation of polluted waters and soils (Ma et al. 1993; Nzihou and Sharrock 2010). Although several studies have indicated that apatite-based materials can be useful for the sorption of organic molecules (Bahdod et al. 2009; Bouyarmane et al. 2010), they have been mostly studied for heavy metal ion removal due to the strong affinity of their surface for cationic species (Baillez et al. 2007; Dybowska et al. 2009). Most recent trends in apatite application to water remediation include the use of natural phosphate minerals as sorbents

(Cao et al. 2004; El Asri et al. 2010), the surface modification of apatite by organic ligands that can enhance the material affinity for metal species (da Silva et al. 2006; Saoiabi et al. 2012) and the formation of apatite-based composites with improved sorption properties (Jang et al. 2008; Achelhi et al. 2011).

In this context, first reports on apatite–iron oxide composites were related to their biomedical (Hou et al. 2009; Wang et al. 2009) and catalytic (Mori et al. 2007) applications. A number of synthetic methodologies have been described over the last few years (Ansar et al. 2012; Mir et al. 2010; Muzquiz-Ramos et al. 2010; Singh et al. 2012; Wakiya et al. 2010). However, only two recent reports are related to remediation methods, taking advantage either of photocatalytic activities of the materials for organic degradation (Yang et al. 2010) or of the apatite affinity for lead ions (Dong et al. 2010). However, none of these studies demonstrate the benefits of iron oxide incorporation in the material recovery after the remediation process. With the purpose of demonstrating the benefits of associating apatite and iron oxide at the nanoscale, we have performed a detailed study of magnetite–hydroxyapatite (Fe$_3$O$_4$–HAp) nanocomposites. The powder's affinity for aqueous lead ions could be correlated with their chemical and structural characterizations. The magnetic characterization supported the existence of a strong apatite–iron oxide interface that allowed the full recovery of the composite powder after lead sorption by application of an external magnetic field. This work has been carried out at University Pierre et Marie Curie (Paris, France) between November 2011 and May 2012.

Materials and methods

Synthesis of the nanocomposite powders

Magnetite (Fe$_3$O$_4$) nanoparticles were prepared following the co-precipitation method. Fe(II) sulfate and Fe(III) nitrate were dissolved in deionized water in a 1:2 molar ratio. The resulting solution was added dropwise to a solution of NaOH (2 mol L^{-1}) under N$_2$ atmosphere at room temperature, producing a dark precipitate. After vigorous mechanical stirring for 30 min, the magnetite (Fe$_3$O$_4$) nanoparticles were recovered by magnetic separation and washed repeatedly with deionized water until a neutral pH is reached and then redispersed into an aqueous suspension (100 mL). The magnetic apatite nanocomposites were obtained via a co-precipitation technique (El Hammari et al. 2007). At 25 °C, Ca(OH)$_2$ (7.4 g, 0.1 mol) powder was first dissolved in an ethanol–water mixture (50:50 v/v, 100 mL) and stirred for 3 h. The magnetic suspension was mixed with NH$_4$H$_2$PO$_4$ (6.9 g, 0.06 mol)

under sonication (at 160 W) for 0.5 h and then added to the Ca(OH)$_2$ solution. The final suspension was aged for 24 h under Argon and then filtered and dried at 100 °C under vacuum overnight. Samples were named after the Fe$_3$O$_4$:HAp molar ratio FeH$_x$.

Pb(II) sorption experiments

The starting Pb(II) solutions (0–1,500 mg L^{-1}) were prepared by dissolution of Pb(NO$_3$)$_2$ salts in deionized water with pH adjusted to 5 by HNO$_3$ addition. For sorption studies, a series of 200-mL glass flasks were filled with 50 mL of Pb(II) solutions. A fixed amount of FeH$_x$ materials (0.1 g) was added into each flask and stirred (200 rpm) for 24 h at 25 °C, to ensure complete sorption equilibrium. A magnet (from MAG NETS, attractive force 295 kg) was placed on the side of the flask, while the solution was removed, to keep the composite on the vessel wall. The Pb(II) content of the supernatant was analyzed by flame atomic absorption spectrometry (FAAS, THERMO Solaar S, detection limit 0.1 ppm for Pb). All experiments were performed in triplicate. For recovery experiment, the composite was added into 50 mL deionized water and stirred (200 rpm) for 24 h at 25 °C. The solution was removed, while the powder was retained in the flask by contact with the magnet. After the magnet was withdrawn, the powder was dried at 50 °C under vacuum overnight. The recovery rate was calculated according to the resulting weight of the powder.

Lead sorption isotherms were analyzed using the non-linear fitting of experimental data with the Langmuir equation

$$q_e = q_{max} \frac{kC_e}{1 + kC_e}$$

where q_e is the amount of Pb(II) adsorbed at equilibrium (mg g^{-1}), q_{max} is the maximum quantity of Pb(II) per unit weight of adsorbent to form a complete monolayer on the surface (mg g^{-1}), k is the Langmuir constant (L g^{-1}), which is related to the binding energy of the Pb(II) to the active site and C_e is the equilibrium concentration (mg g^{-1}).

Characterization techniques

The crystalline phases of the nanocomposites before and after Pb(II) sorption were characterized using a powder X-ray diffractometer (XRD) (Philips PW131 diffractometer), in a 2θ range from 10° to 70°. The morphology and size of HAp and FeH$_x$ nanoparticles were examined using a transmission electron microscopy (TEM) (Tecnai spirit G2) operating at 100 kV, a high-resolution transmission electron microscope (HR-TEM) (JEOL JEM-2010 UHR)

operating at 200 kV and a field emission scanning electron microscope (FEG-SEM) (Hitachi SU70) operating at 5 kV. The samples for the microscopy studies were coated with a thin platinum film about 5 Å in thickness on the surface in a sputter coater (Balzers Union SCD 40). The N_2
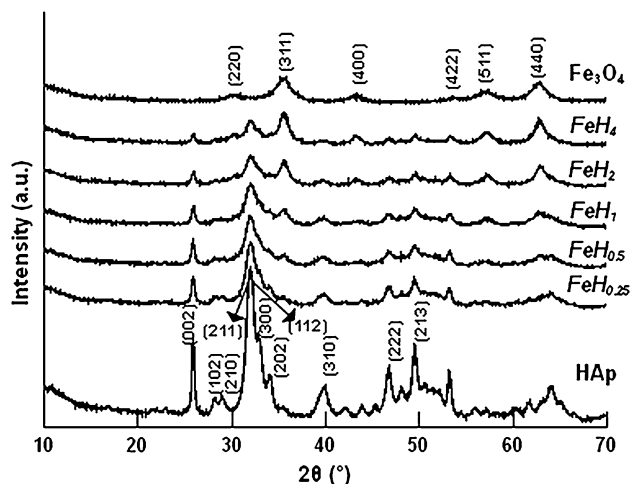

Fig. 1 XRD patterns of Fe_3O_4, HAP and selected nanocomposites

adsorption–desorption isotherms for dried powders were recorded by multipoint N_2 gas sorption experiments at 77 K using a Belsorb instrument. The specific surface areas were calculated according to the Brunauer–Emmett–Teller (BET) method in the relative pressure range from 0.05 to 0.25.

Variable temperature direct current (dc) magnetizations were collected on Quantum Design PPMS-5S or MPMS-XL SQUID magnetometers equipped with a 5 or a 7 T dc magnet, respectively. The hysteresis curves were measured to obtain coercive field and the saturation magnetization at 20 and 300 K. The zero field cooled–field cooled (ZFC–FC) measurements were performed at 100 Oe and in the temperature range between 350 and 2 K. The sample was introduced into the magnetometer at 300 K and heated to 350 K. For the ZFC curve, temperature was lowered under zero field to 10 K first at a 5 K/min rate and then at a 1 K/min below 10 K. After thermal stabilization of the sample at 2 K, a dc magnetic field of 100 Oe was applied and the ZFC magnetization of the sample was recorded as the temperature was raised at a 1 K/min rate between 2 and 10 K and at a 2 K/min rate above 10 K. The sample was then cooled again to 2 K under the magnetic field of 100
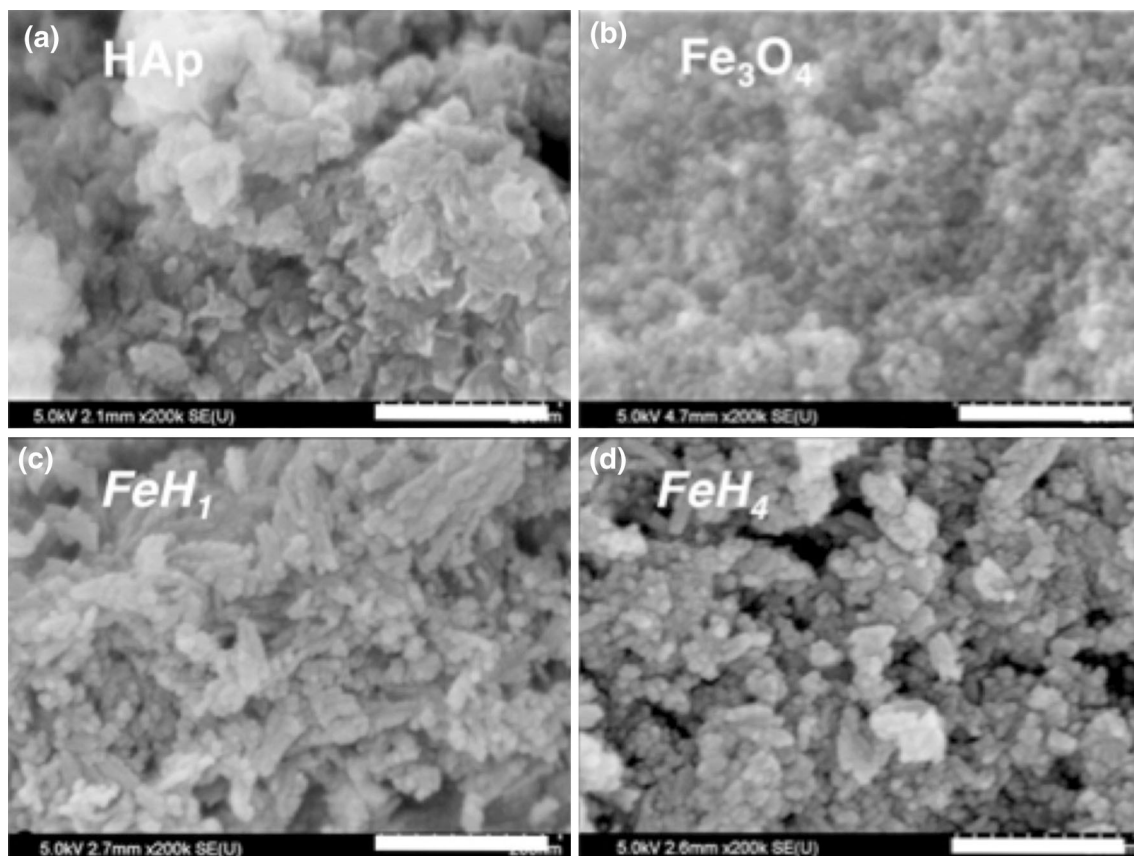

Fig. 2 SEM-FEG images of **a** HAp, **b** Fe_3O_4, **c** FeH_1 and **d** FeH_4 (scale bar = 200 nm)
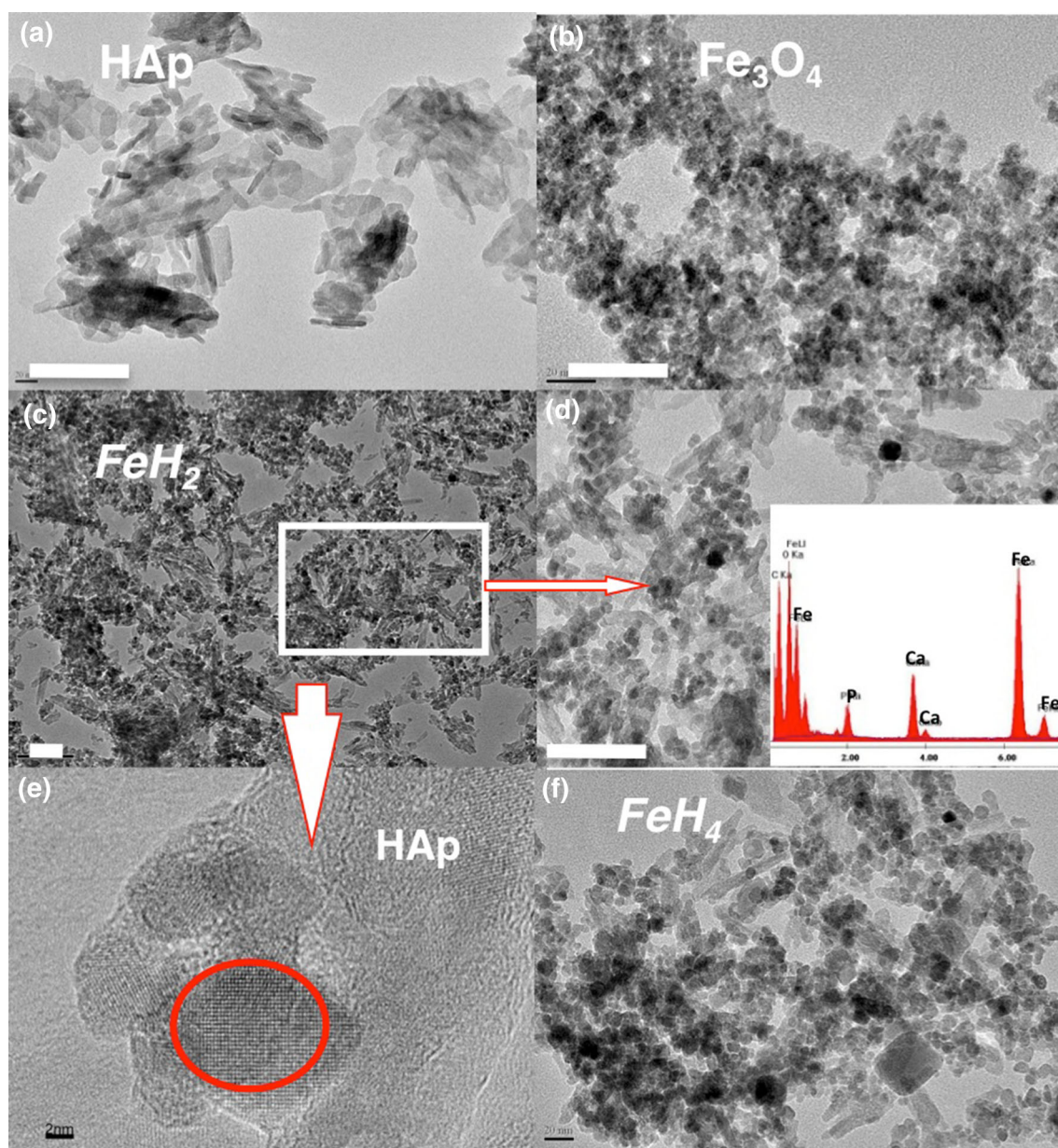
Fig. 3 TEM images of the nanoparticles: **a** HAp, **b** Fe$_3$O$_4$, **c–e** FeH$_2$ (*insert*: EDX spectra) and **f** FeH$_4$ (scale bar = 200 nm, except (**e**) 2 nm)

Oe, and the FC curve was obtained in the same conditions as for ZFC curve.

Results and discussion

Magnetite–hydroxyapatite nanocomposite characterization

The XRD patterns of the FeH$_x$ composites together with the pure HAp and Fe$_3$O$_4$ powders are shown in Fig. 1. The well-resolved diffraction peaks of pure HAp correspond to the reference hydroxyapatite patterns (JCPDS 09-0432). In particular, the major peaks of HAp corresponding to (002), (211), (112), (300), (202), (310), (222) and (213) planes can be clearly seen in all the FeH$_x$ composites. As the Fe$_3$O$_4$:HAp ratio increases, the intensity of the diffraction peaks at $2\theta \approx 35°$, 57° and 63° corresponding to the (311), (511) and (440) planes of the magnetite Fe$_3$O$_4$ structure (JCPDS 75-1609) increases. The increase of other peaks, especially the (220) diffraction expected at $2\theta \approx 31°$ is more difficult to follow as some overlap exists with HAp diffraction peaks. It is worth noting that the presence of γ-Fe$_2$O$_3$ particles (JCPDS-39-1346), which can result from
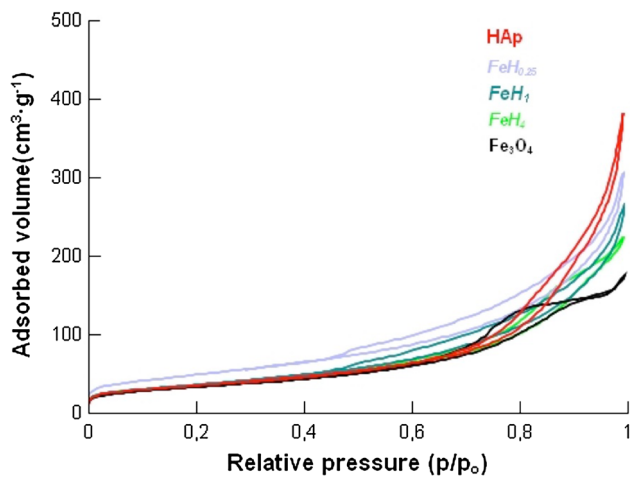
Fig. 4 N_2-sorption isotherms for selected powders

powder drying, cannot be fully put aside as the XRD patterns of two iron oxide phases differ mainly by small intensity peaks. Noticeably, the HAp diffraction peaks are still visible for the FeH_4 sample and no additional diffraction peaks are apparent that could have correspondence with another calcium phosphate phase. This suggests that the presence of Fe_3O_4 does not interfere with the precipitation of the HAp phase.

The morphology and particle size of the samples were investigated in detail by FEG-SEM, as shown in Fig. 2. Figure 2a shows HAp agglomerates, composed of rod-like particles with 50 nm in length and sometimes platelets with an average size of 80 nm. Fe_3O_4 nanoparticles exhibiting uniform spherical shape with a mean particle size of 10 nm form dense aggregates (Fig. 2b). Starting from HAp, addition of low amount of Fe_3O_4 leads to the observation of these small spherical nanoparticles, while the HAp particles appear more dispersed (Fig. 2c). With increasing Fe_3O_4:HAp molar ratio, the density of magnetic particles

increases but an inter-particular porosity is still evidenced (Fig. 2d and ESM-1).

TEM images (Fig. 3) provide more details about the organization of the composite powders. The HAp (Fig. 3a) and iron oxide particles (Fig. 3b) have distinct size, morphology and contrast so that they can be easily distinguished in the different FeH_x composites (Fig. 3c–f and ESM-2). In all situations, Fe_3O_4 colloids uniformly surround HAp particles. The energy-dispersive X-ray (EDX) spectra, inset of Fig. 3d, provide evidence that the Ca/P molar ratio of the composite phase is close to 1.67, which corresponds to the stoichiometric composition of HAp. Figure 3d is an enlarged TEM picture of FeH_2 composite at high magnification, which clearly shows the good dispersion of Fe_3O_4 colloids within the HAp aggregates. In addition, the observation of continuous lattice fringes across individual FeH_x nanorods in HRTEM images (Fig. 3e) indicates the possible coexistence of the well-crystallized phases of HAp and Fe_3O_4 within a same grain.

Figure 4 shows the nitrogen sorption isotherms of the FeH_x composites, together with the HAp and Fe_3O_4 pristine powders. The Fe_3O_4 powder exhibits a type IV isotherm with a H1 hysteresis according to IUPAC (Singh et al. 1985), which reflects inter-particular porosity due to the packing of spherical particles of size of 8–15 nm. FeH_x isotherms have a similar shape to that of HAp materials and can be classified as type IV isotherms with a type H3 hysteresis (Singh et al. 1985). This can be attributed to the platelet-like shape of HAp nanoparticles, as already observed in zirconia–HAp nanocomposites (Achelhi et al. 2011). In the high-p/p_0 pressure domain, the HAp and FeH_x isotherms do not exhibit a well-defined plateau, reflecting the absence of a closed mesoporosity.

These variations are also reflected by the modifications of their specific surface area (S_{BET}) (Table 1). As a comparison with the starting HAp, $FeH_{0.25}$ exhibits a sharp increase in S_{BET} (from ca. 125 to 175 m^2 g^{-1}). In the

Table 1 Fe_3O_4 content and specific surface area (S_{BET}) of pure phases and composite powders

	HAp:Fe_3O_4 molar ratio	Fe_3O_4 (wt%)	S_{BET} (m^2*g^{-1})	q_{max}^a [$q_{max-HAp}$][b] (mg g^{-1})	k [k_{HAp}] (L g^{-1})	R^2
HAP	–	0	125	246 [246]	4.5 [4.5]	0.984
$FeH_{0.25}$	4	5.48	175	496 [524]	1.0 [1.0]	0.996
$FeH_{0.5}$	2	10.39	170	–	–	–
FeH_1	1	18.83	160	412 [507]	0.8 [1.1]	0.993
FeH_2	0.5	31.69	140	372 [541]	0.8 [1.1]	0.978
FeH_4	0.25	48.13	125	294 [566]	0.8 [1.5]	0.986
Fe_3O_4	–	100	105	–	–	–

Maximum removal capacity q_{max} and Langmuir constant k. R^2 corresponds to the correlation coefficient obtained from the nonlinear fitting procedure. [$q_{max-HAp}$] and [k_{HAp}] calculated per g of HAp

[a] ±15 mg g^{-1}, [b] ±20 mg g^{-1}

1178

Int. J. Environ. Sci. Technol. (2015) 12:1173–1182

composite structures, inter-particular porosity may arise from three types of populations: Fe_3O_4–Fe_3O_4, Fe_3O_4–HAp and HAp–HAp. As observed for $FeH_{0.25}$, the Fe_3O_4–HAp interface becomes predominant over HAp–HAp at low iron oxide content, indicating that the magnetic particles

efficiently disperse the apatite particles in the composite structure. The Fe_3O_4–Fe_3O_4 population is expected to grow at the expense of the Fe_3O_4–HAp population with increasing iron oxide content. This is also reflected by the specific surface area data since for Fe_3O_4:HAp above 0.25, the S_{BET} value decreases with increasing iron oxide amount.

The magnetic properties of the pure Fe_3O_4 nanoparticles and FeH_1 composite powders were first investigated via FC–ZFC measurements (Fig. 5 and ESM-3). For the pure iron oxide powder, no clear maximum of magnetization is observed in the investigated temperature range, indicating a distribution of blockage temperature T_B between 200 and 300 K. In the FeH_1 composite powder, a maximum is observed at ca. 170 K. However, T_{SEP} was found to be ca. 300 K for both systems. Taken together, these data indicate a significant particle size distribution (Chatterjee et al. 2003). For instance, it was calculated that T_B ranges from ca. 200 to 300 K for magnetite particle size ranging from 5 to 15 nm (Yoon 2011). The difference in T_B values between the pure iron oxide and the composite may arise either from decreasing magnetite–magnetite interactions in the composite due to the dispersion of the magnetic particles and/or to the presence of an apatite layer on the iron oxide surface (Morup and Tronc 1994; Roca et al. 2009). Noticeably, investigation of the magnetic properties of the pure HAp revealed a paramagnetic behavior below 22 K, which can be attributed to trace metal impurities in the apatite precursor (ESM-4). Such a behavior explains the unexpected shape of the ZFC curve of FeH_1 at low temperatures. Magnetization versus applied field curves were also recorded for both samples at 20 and 300 K (Fig. 6a, b and ESM-5). For Fe_3O_4, the coercivity Hc is 400 Oe at 20 K and almost zero (i.e., <20 Oe) at 300 K. A similar
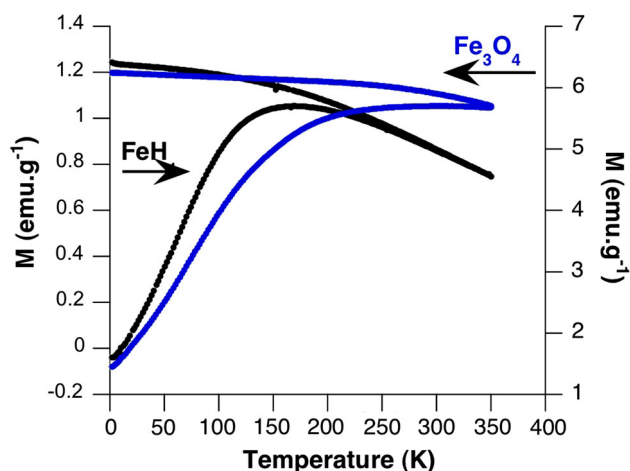

Fig. 5 Magnetization (M) versus temperature FC–ZFC curves of Fe_3O_4 (*blue dots* left-hand axis) and FeH_1 (*black dots* right-hand axis) recorded at 100 Oe
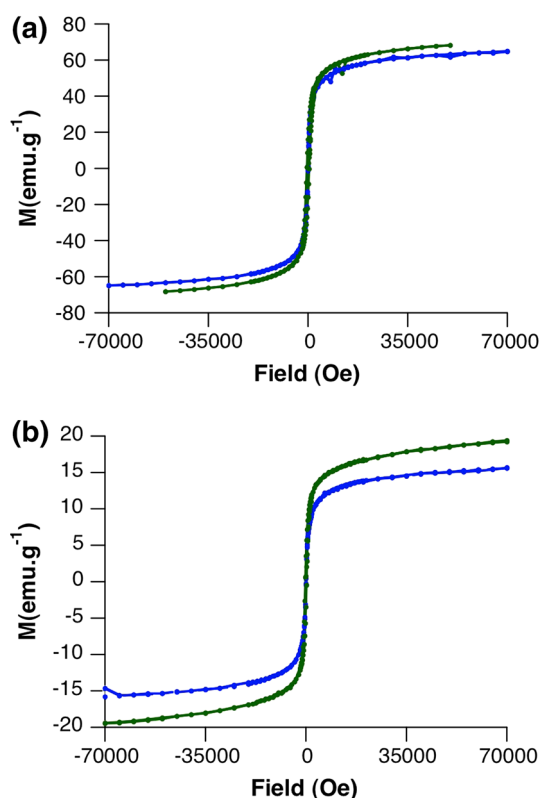

Fig. 6 Magnetization (M) versus applied field hysteresis curves at 20 K (*green dots*) and 300 K (*blue dots*) for **a** Fe_3O_4 and **b** FeH1
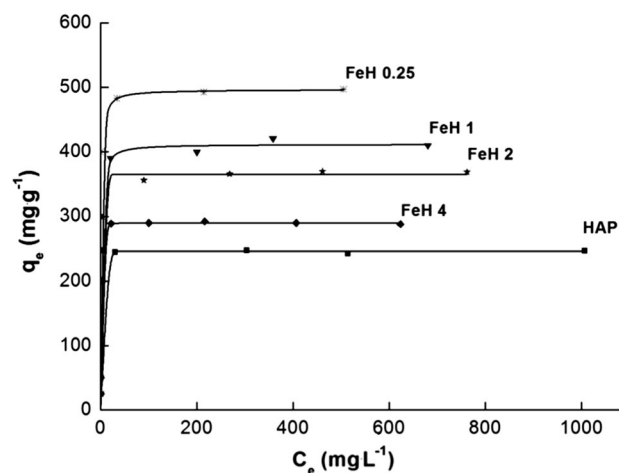

Fig. 7 Pb(II) sorption isotherms on selected materials. *Plain lines* indicate the result of data fitting using the Langmuir equation
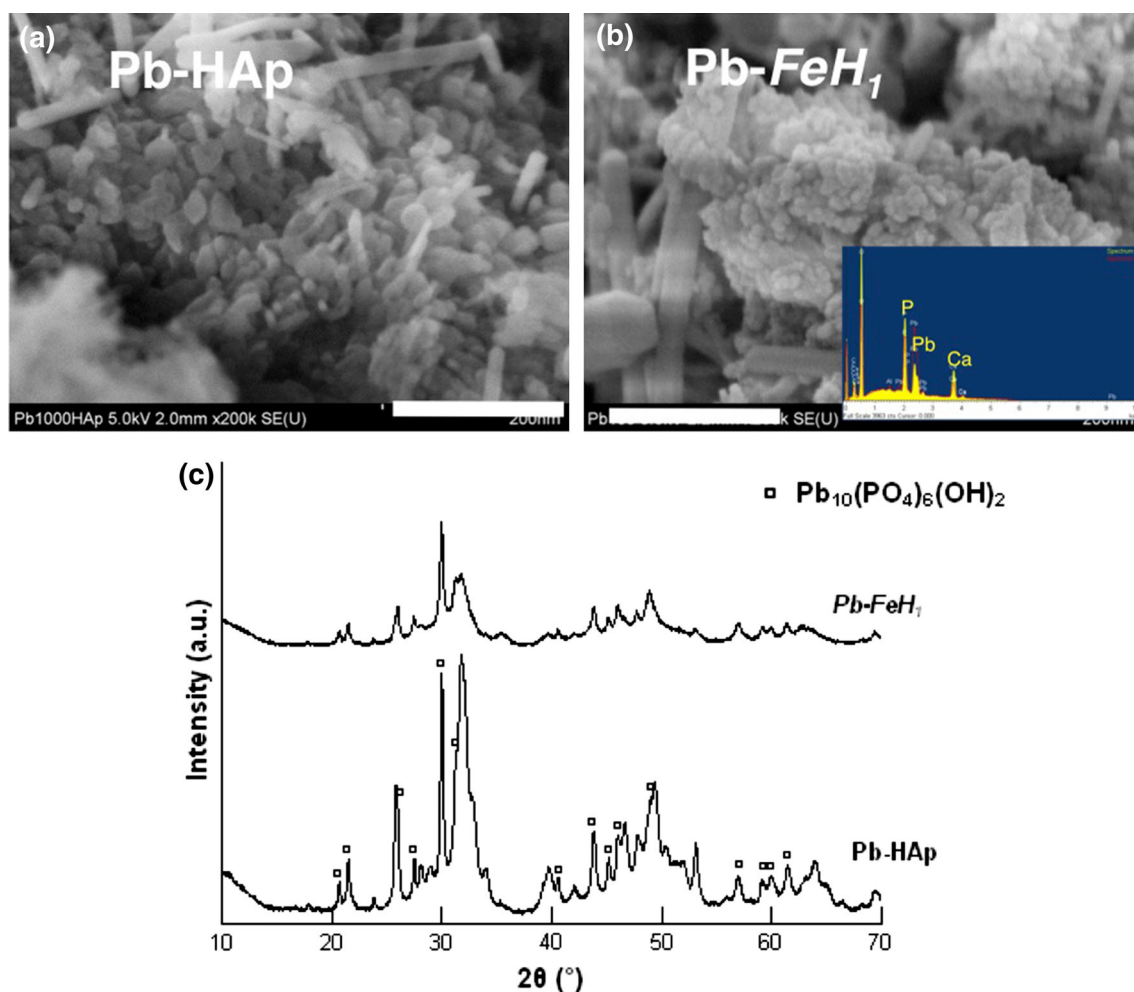
Fig. 8 **a**, **b** FEG-SEM images and **c** XRD patterns of HAp and FeH₁ after Pb(II) sorption. *Insert* EDX spectra of Pb–FeH₁
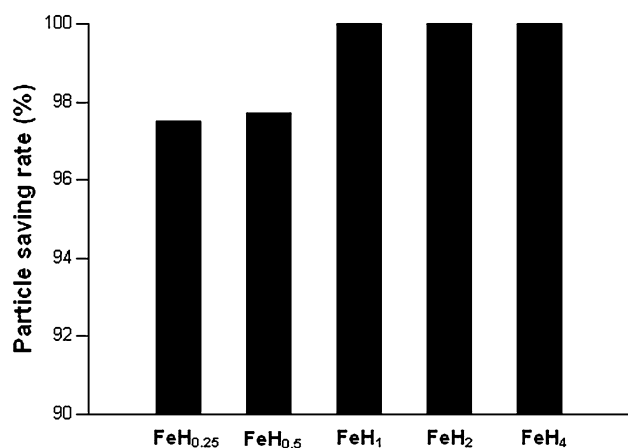

Fig. 9 Magnetic recovery rates for selected composites

trend is observed for FeH₁. This indicates that, for both powders, most iron oxide particles exhibit T_B values below 300 K, strengthening our previous statement about the lack of precision of T_B determination due to particle size dispersity.

Considering saturation magnetization M_s, its value is 65 emu g^{-1} at room temperature for the pure iron oxide powder, which is lower than bulk magnetite at the same temperature (ca. 90 emu g^{-1}) (Vergés et al. 2008) and compares well with reported values for iron oxide particles of similar size (Goya et al. 2003). The FeH₁ composite has a M_s value of 16 emu g^{-1}, which is about 17 % that of pure Fe₃O₄ nanoparticles, being therefore consistent with Fe₃O₄ particles content in the FeH₁ composite.

Pb(II) removal experiments

Pb(II) was selected to investigate the relationship between the surface properties and the heavy metal ion removal ability of FeH$_x$ composites, not only due to its environmental relevance (Abdel-Ghani et al. 2007; Okoye et al. 2010; Saka et al. 2012) but also due to its strong affinity toward apatite. Preliminary kinetics experiments

1180

Int. J. Environ. Sci. Technol. (2015) 12:1173–1182

showed that the sorption equilibrium was reached after 4 h (ESM-6). Fig. 7 presents the lead removal curves obtained at pH 5. First, it is important to point out that Pb(II) removal was almost total (>99 %) at low initial lead content, so that several sorption data overlap in the first part of the plotted isotherms. At high initial lead content, the removal capacity of composites is significantly enhanced compared to pure HAp, especially at low magnetite content. Noticeably, the pure Fe_3O_4 nanoparticles show no Pb(II) removal capability (data not shown). The maximum removal capacity q_{max} and Langmuir constant k were calculated for each sample, and the results are presented in Table 1. In all situations, the correlation coefficient R^2 for the nonlinear fitting was found ≥ 0.978, suggesting that Langmuir model is well-adapted to describe the sorption process and therefore that lead sorption occurs via monolayer coverage on the adsorbent surface.

Interestingly, $FeH_{0.25}$ has a maximum capacity (ca. 500 mg g^{-1}) much higher than pure HAp (ca. 250 mg g^{-1}), and the maximum capacity decreases to 290 mgThe following references are not cited in text: [CR6 CR29 CR35 CR60]{CR6} LD Cameron, H Leventhal, R Love, (1998){CR29} K Leithner, A Maar, M Fischer-Kern, E Hilger, H Löffler-Stastka, E Ponocny-Seliger, (2004){CR35} SM Miller, (1995){CR60} Z Zlotogorski, O Tadmor, E Duniec, R Rabinowitz, Y Diaman, (1995)g^{-1} with increasing iron content. It is interesting to evaluate the influence of the composite structure on the surface reactivity of hydroxyapatite by calculating the removal capacity per gram of HAp. In this situation, the maximum capacity is quite similar for all composites (>500 mgThe following references are not cited in text: [CR6 CR29 CR35 CR60]{CR6} LD Cameron, H Leventhal, R Love, (1998){CR29} K Leithner, A Maar, M Fischer-Kern, E Hilger, H Löffler-Stastka, E Ponocny-Seliger, (2004){CR35} SM Miller, (1995){CR60} Z Zlotogorski, O Tadmor, E Duniec, R Rabinowitz, Y Diaman, (1995)g^{-1}) and two times higher than that of pure HAp. In parallel, the value of k slightly decreases from pure HAp to $FeH_{0.25}$ and remains constant with Fe_3O_4:HAp molar ratio when calculated over the whole composite weight or per gram of HAp. It is also interesting to note that attempts to use a Freundlich-type model for the FeH_x materials led to unreliable parameters. This indicates that the composite surface is homogeneous toward lead sorption, i.e., Pb^{2+} interacts only with one kind of particles, namely apatite. Taken together, these data suggest that the apatite phase is responsible for the lead sorption process and that the presence of iron oxide increases the HAp particle dispersion but does not significantly show any impact on the surface affinity of the HAp phase for Pb^{2+}.

Post-sorption powder analysis and recovery

To investigate further the lead removal process, the HAp and FeH_x samples were characterized after the Pb(II) sorption experiments (samples Pb–HAp and Pb–FeH_x, respectively). The FEG-SEM images of the Pb–HAp and Pb–FeH_x particles are presented in Fig. 8a, b, respectively. Large needle-like particles can be seen on the particle surfaces, whose size is 50–300 nm in length and 20–50 nm in width. The related EDX spectrum clearly shows the presence of Pb in all the samples. The XRD diffractograms show distinct peaks that can be attributed to hydroxypyromorphite with a formula of $Pb_{10}(PO_4)_6(OH)_2$ (JCPDS 02-0700) (Fig. 8c). This is in agreement with previous reports from the literature, indicating that HAp is transformed into hydroxypyromorphite via the sorption of Pb(II) followed by the cation exchange reaction between Pb(II) ions in aqueous solution and Ca(II) ions of HAp in the composites (Lower et al. 1998).

Finally, the efficiency of the magnetically induced recovery of the Pb–FeH_x materials was investigated. As shown in Fig. 9, the composite shows a very good particle recovery rate after stirring for 24 h, with 100 % efficiency for Fe_3O_4:HAp ≥ 1. This success implies that each apatite particle is associated with a sufficient number of magnetite particles to be attracted by the magnetic field. This also explains why a minimum Fe_3O_4:HAp ratio is required to obtain full recovery. These experiments are also in agreement with the homogeneous dispersion of the magnetite particles in the HAp network. Finally, they indicate the existence of a strong interaction between the apatite and iron oxide particles, which may otherwise have left the HAp surface under the magnetic field attractive strength. Interestingly, the full powder recovery indicates that hydroxypyromorphite is also removed by application of the magnetic field, in agreement with SEM images showing that this phase is formed at the surface of the particles.

Conclusion

This work describes Fe_3O_4–HAp nanocomposites combining high capacity toward lead ion removal and efficient magnetic recovery. These materials combine two mineral phases that are biodegradable and non-toxic, and the preparation process is of low environmental impact and should be easily scaled up. For all these reasons, these novel sorbents appear very promising for heavy metal removal. However, it should be possible to extend the field of application of these materials by taking advantage of the intrinsic sorption properties of the iron oxide phase for other metals, such as As(III)/As(V) species or organic matter.

References

Abdel-Ghani NT, Hefny M, El-Chaghaby GAF (2007) Removal of lead from aqueous solution using low cost abundantly available adsorbents. Int J Environ Sci Tech 4(1):67–74

Achelhi K, Masse S, Laurent G, Roux C, Laghzizil A, Saoiabi A, Coradin T (2011) Ultrasound-assisted synthesis of mesoporous zirconia-hydroxyapatite nanocomposites and their dual surface affinity for $Cr^{3+}/Cr_2O_7^{2-}$ ions. Langmuir 27(24):15176–15184

Ansar EB, Ajeesh M, Yokogawa Y, Wunderlich W, Varma V (2012) Synthesis and characterization of iron oxide embedded hydroxyapatite bioceramics. J Am Ceram Soc 95(9):2695–2699

Bahdod A, El Asri S, Saoiabi A, Coradin T, Laghzizil A (2009) Adsorption of phenol from an aqueous solution by selected apatite adsorbents: kinetic process and impact of the surface properties. Water Res 43(2):313–318

Baillez S, Nzihou A, Bernache-Assolant D, Champion E, Sharrock P (2007) Removal of aqueous lead ions by hydroxyapatite: equilibria and kinetic processes. J Hazard Mater 139(3):443–446

Benjamin MM, Sletten RS, Bailey RP, Bennett T (1996) Sorption and filtration of metals using iron-oxide-coated sand. Water Res 30(11):2609–2620

Booker NA, Keir D, Priestley A, Rithchie CD, Sudarmana DL, Woods MA (1991) Sewage clarification with magnetite particles. Water Sci Technol 23(7–9):1703–1712

Bouyarmane H, El Asri S, Rami A, Roux C, Mahly MA, Saoiabi A, Coradin T, Laghzizil A (2010) Pyridine and phenol removal using natural and synthetic apatites as low cost sorbents: influence of porosity and surface interactions. J Hazard Mater 181(1–3):736–741

Cao X, Ma LQ, Rhue DR, Appel CS (2004) Mechanisms of lead, copper, and zinc retention by phosphate rock. Environ Pollut 131(3):435–444

Chatterjee J, Haik Y, Chen CJ (2003) Size dependent magnetic properties of iron oxide nanoparticles. J Magn Magn Mater 257(1):113–118

da Silva OG, da Silva Filho EC, da Fonseca MG, Arakaki LNH, Airoldi C (2006) Hydroxyapatite organofunctionalized with silylating agents to heavy cation removal. J Colloid Interface Sci 302(2):485–491

Dong L, Zhu Z, Qiu Y, Zhao J (2010) Removal of lead from aqueous solution by hydroxyapatite/magnetite composite adsorbent. Chem Eng J 165(3):827–834

Dybowska A, Manning DAC, Collins MJ, Wess T, Woodgate S, Valsami-Jones E (2009) An evaluation of the reactivity of synthetic and natural apatites in the presence of aqueous metals. Sci Tot Environ 407(8):2953–2965

El Asri S, Laghzizil A, Coradin T, Saoiabi A, Alaoui A, M'hamedi R (2010) Conversion of natural phosphate rock into mesoporous hydroxyapatite for heavy metals removal from aqueous solution. Colloids Surf A Physicochem Eng Asp 362(1–3):33–38

El Hammari L, Merroun H, Coradin T, Cassaignon S, Laghzizil A (2007) Mesoporous hydroxyapatites prepared in ethanol–water media: structure and surface properties. Mater Chem Phys 104(2–3):448–453

Goya GF, Berquo TS, Fonseca FC, Morales MP (2003) Static and dynamic magnetic properties of spherical magnetite nanoparticles. J Appl Phys 94:3520–3528

Hou CH, Hou SM, Hsueh YS, Lin J, Wu HC, Lin FH (2009) The in vivo performance of biomagnetic hydroxyapatite nanoparticles in cancer hyperthermia therapy. Biomaterials 30(23–24):3956–3960

Jang SH, Min BG, Jeong YG, Lyoo WS, Lee SC (2008) Removal of lead ions in aqueous solution by hydroxyapatite/polyurethane composite foams. J Hazard Mater 152(3):1285–1292

Lower SK, Maurice PA, Traina SJ, Carlson EH (1998) Aqueous Pb sorption by hydroxylapatite: application of atomic force microscopy to dissolution, nucleation, and growth studies. Am Miner 83:147–158

Ma QY, Traina SJ, Logan TJ, Ryan JA (1993) In-situ lead immobilization by apatite. Environ Sci Technol 27:1803–1810

Mir A, Mallik D, Bhattacharya S, Mahata D, Sinha A, Nayar S (2010) Aqueous ferrofluids as templates for magnetic hydroxyapatite nanocomposites. J Mater Sci Mater Med 21(8):2365–2369

Mori K, Kanai S, Hara T, Mizugaki T, Ebitani K, Jitsukawa K, Kaneda K (2007) Development of ruthenium-hydroxyapatite-encapsulated superparamagnetic γ-Fe_2O_3 nanocrystallites as an efficient oxidation catalyst by molecular oxygen. Chem Mater 19(6):1249–1256

Morup S, Tronc E (1994) Superparamagnetic relaxation of weakly interacting particles. Phys Rev Lett 72(20):3278–3281

Muzquiz-Ramos EM, Cortés-Hernandez DA, Escobedo-Bocardo J (2010) Biomimetic apatite coating on magnetite particles. Mater Lett 64(9):17–19

Nzihou A, Sharrock P (2010) Role of phosphate in the remediation and reuse of heavy metal polluted wastes and sites. Waste Biomass Valor 1(1):163–174

Okoye AI, Ejikeme PM, Onukwuli OD (2010) Lead removal from wastewater using fluted pumpkin seed shell activated carbon: adsorption modelling and kinetics. Int J Environ Sci Tech 7(4):793–800

Oliveira LCA, Rios RVRA, Fabris JD, Garg V, Sapag K, Lago RM (2002) Activated carbon/iron oxide magnetic composites for the adsorption of contaminants in water. Carbon 40(12):2177–2183

Oliveira LCA, Rios RVRA, Fabris JD, Garg V, Sapag K, Lago RM (2003) Clay-iron oxide magnetic composites for the adsorption of contaminants in water. Appl Clay Sci 22(4):169–177

Oliveira LCA, Petkowicz DI, Smaniotto A, Pergher SBC (2004) Magnetic zeolites: a new adsorbent for removal of metallic contaminants from water. Water Res 38(17):3699–3704

Roca AG, Niznansky D, Poltierova-Vejpravova J, Bittova B, Gonzalez-Fernandez MA, Serna CJ, Morales MP (2009) Magnetite nanoparticles with no surface spin canting. J Appl Phys 105(11):114309

Saka C, Sahin O, Kucuk M (2012) Applications of agricultural and forest waste adsorbents fort he removal of lead(II) from contaminated waters. Int J Environ Sci Tech 9(2):379–394

Saoiabi S, El Asri S, Saoiabi A, Laghzizil A, Ackerman JL, Coradin T (2012) Lead and zinc removal from aqueous solutions by aminotriphosphonate-modified converted natural phosphates. Chem Eng J 211–212:233–239

Singh KS, Everett DH, Haul RW, Moscou L, Pierotti RA, Rouquérol J, Siemieniewska T (1985) Reporting physisorption data for gas/solid systems with special reference to the determination of surface area and porosity. Pure Appl Chem 57(11):603–619

Singh RK, El-Fiqi AM, Patel KD, Kim HW (2012) A novel preparation of magnetic hydroxyapatite nanotubes. Mater Lett 75:130–133

Vergés MA, Costo R, Roca AG, Marco JF, Goya GF, Serna CJ, Morales MP (2008) Uniform and water stable magnetite

1182

Int. J. Environ. Sci. Technol. (2015) 12:1173–1182

nanoparticles with diameters around the monodomain–multido-main limit. J Phys D Appl Phys 41(13):134003

Wakiya N, Yamasaki M, Adachi T, Inukai A, Sakamoto N, Fu D, Sakurai O, Shinozaki K, Suzuki H (2010) Preparation of hydroxyapatite-ferrite composite particles by ultrasonic spray pyrolysis. Mater Sci Eng, B 173(1–3):195–198

Wang D, Duan X, Zhang J, Yao A, Zhou L, Huang W (2009) Fabrication of superparamagnetic hydroxyapatite with highly ordered three-dimensional pores. J Mater Sci 44(15):4020–4025

Yang Z, Gong X, Zhang C (2010) Recyclable Fe_3O_4/hydroxyapatite composite nanoparticles for photocatalytic applications. Chem Eng J 165(1):117–121

Yoon S (2011) Determination of the temperature dependence of the magnetic anisotropy constant in magnetite nanoparticles. J Korean Phys Soc 59(5):3069–3073